

# Spectroscopic Indications of Tunnel Barrier Charging as the Switching Mechanism in Memristive Devices

Benedikt Arndt,\* Francesco Borgatti, Francesco Offi, Monifa Phillips, Pedro Parreira, Thorsten Meiners, Stephan Menzel, Katharina Skaja, Giancarlo Panaccione, Donald A. MacLaren, Rainer Waser, and Regina Dittmann\*

Resistive random access memory is a promising, energy-efficient, low-power “storage class memory” technology that has the potential to replace both flash storage and on-chip dynamic memory. While the most widely employed systems exhibit filamentary resistive switching, interface-type switching systems based on a tunable tunnel barrier are of increasing interest. They suffer less from the variability induced by the stochastic filament formation process and the choice of the tunnel barrier thickness offers the possibility to adapt the memory device current to the given circuit requirements. Heterostructures consisting of a yttria-stabilized zirconia (YSZ) tunnel barrier and a praseodymium calcium manganite (PCMO) layer are employed. Instead of spatially localized filaments, the resistive switching process occurs underneath the whole electrode. By employing a combination of electrical measurements, in operando hard X-ray photoelectron spectroscopy and electron energy loss spectroscopy, it is revealed that an exchange of oxygen ions between PCMO and YSZ causes an electrostatic modulation of the effective height of the YSZ tunnel barrier and is thereby the underlying mechanism for resistive switching in these devices.

## 1. Introduction


Resistance random access memory (ReRAM) has drawn considerable attention as a replacement for current nonvolatile memories.<sup>[1]</sup> It is based on the different resistance states that can be set by specific electrical stimulation of a large variety of binary and complex transition metal oxides, including

titanates, zirconates,<sup>[2–4]</sup> and manganites.<sup>[5–9]</sup> For many of these systems, the typically bipolar resistive switching arises from redox processes that are induced by a voltage-driven movement of oxygen vacancies within a spatially confined filament region that evolves initially during a so-called electroforming process.<sup>[1]</sup> Homogenous interface-type resistive switching, in contrast, suffers less from the variability of the stochastic filament formation process and is characterized instead by a scaling of the device currents with the electrode area in both the high (HRS) and low resistive state (LRS).<sup>[10–14]</sup> A variety of mechanisms have been proposed as being responsible for the interface-type resistive switching phenomenon, such as field driven movement of oxygen vacancies,<sup>[7,15–23]</sup> trapping of charge carriers (holes or electrons),<sup>[9,24]</sup> and an interfacial Mott transition.<sup>[25–29]</sup>

In this work, we investigated an interface-type resistive switching system based on the mixed valence manganite  $\text{Pr}_{1-x}\text{Ca}_x\text{MnO}_3$ .<sup>[30]</sup> Manganite thin films generally form an ohmic contact with noble metals, such as Pt and Au,<sup>[30,31]</sup> while a nonlinear current–voltage relationship is observed when applying oxidizable metals, such as Al, Ti, or Ta.<sup>[9,30]</sup> Non-noble metals typically form an interface oxide layer that governs the resistance of the whole stack.<sup>[22,32–34]</sup>

B. Arndt, T. Meiners, Dr. S. Menzel, Dr. K. Skaja, Prof. R. Waser, Prof. R. Dittmann  
Peter Grünberg Institute  
Research Center Jülich  
Wilhelm-Johnen-Straße, Jülich 52425, Germany  
E-mail: b.arndt@fz-juelich.de; r.dittmann@fz-juelich.de

Dr. F. Borgatti  
Consiglio Nazionale delle Ricerche  
Istituto per lo Studio dei Materiali Nanostrutturati (CNR-ISMN)  
via P. Gobetti 101, I-40129 Bologna, Italy

 The ORCID identification number(s) for the author(s) of this article can be found under <https://doi.org/10.1002/adfm.201702282>.

© 2017 The Authors. Published by WILEY-VCH Verlag GmbH & Co. KGaA, Weinheim. This is an open access article under the terms of the Creative Commons Attribution License, which permits use, distribution and reproduction in any medium, provided the original work is properly cited.

DOI: 10.1002/adfm.201702282

Prof. F. Offi  
CNISM and Dipartimento di Scienze  
Via della Vasca Navale 84, I-00146 Rome, Italy

M. Phillips, Dr. P. Parreira, Dr. D. A. MacLaren  
SUPA  
School of Physics and Astronomy  
The University of Glasgow  
Glasgow G12 8QQ, UK

Dr. G. Panaccione  
CNR–Istituto Offi cina dei Materiali (IOM)  
Laboratorio TASC  
S.S.14, Km 163.5, I-34149 Trieste, Italy

Prof. R. Waser  
Institute of Materials in Electrical Engineering and Information  
Technology  
RWTH Aachen University  
52056 Aachen, Germany

For the Ti/PCMO system it has been shown that the amount of fully oxidized Ti ions in the interface oxide determines the different resistive states. A model in which  $\text{TiO}_x$  acts as a tunnel barrier and praseodymium calcium manganite (PCMO) is characterized by a field enhanced polaron hopping conduction mechanism shows that the  $I$ - $V$  characteristics of the HRS and the formed state are dominated by the tunnel barrier, whereas it plays a minor role in the LRS and the pristine state characteristics.<sup>[35]</sup>

A similar system, developed by Unity Semiconductor, is the so-called “tunnel ReRAM”, where an insulating oxide (TO) is intentionally deposited between a noble metal top electrode and a conductive metal oxide (CMO).<sup>[36,37]</sup> In principle, such a system offers the advantage that either the area of the device or the thickness of the tunnel barrier (or both) can be varied to tailor the currents in the respective resistive states according to the requirements of a given circuit. The authors of this study attribute the switching effect to an exchange of oxygen between the CMO and the TO, facilitated by an exponential increase in the mobility of oxygen ions within high electric fields. As oxygen ions give rise to an ionic space charge, they modulate the barrier height and hence the tunneling current, which has been considered for various systems.<sup>[36,38,39]</sup> However, direct experimental evidence of this effect has yet to be demonstrated conclusively.

In this paper, we have investigated the origin of the resistive switching mechanism for ReRAM devices incorporating yttria-stabilized zirconia (YSZ) as a TO and epitaxially grown  $\text{Pr}_{0.48}\text{Ca}_{0.52}\text{MnO}_3$  (PCMO) as the CMO layer. To this end, we have performed static and in operando hard X-ray core-level photoelectron spectroscopy (HAXPES) to probe the buried YSZ/PCMO interface region, where oxygen migration is expected. Thanks to the larger probing depth (>10 nm) achievable with respect to conventional X-ray photoelectron spectroscopy, HAXPES provides an excellent, nondestructive approach to probe chemical changes and charging effects of interfaces buried inside layered heterostructures, in addition to the bulk electronic structure of the materials.<sup>[40–44]</sup> In particular, in operando HAXPES performed on a device electrically biased in situ provides an opportunity to correlate very strictly the resistive switching effects to the electronic structure and the electrical potential of the probed volume.<sup>[45–47]</sup>

The HAXPES investigations are supplemented by scanning transmission electron microscopy-electron energy loss spectroscopy (STEM-EELS), which provides complementary structural and chemical information with high spatial resolution throughout the device stack. Our results provide direct spectroscopic evidence of the build-up of space charges at the YSZ/PCMO interface. We reveal that this is related to an exchange of oxygen ions between PCMO and YSZ and causes a modulation of the effective height of the YSZ tunnel barrier and is thereby the key underlying mechanism for the resistance change in these devices.

## 2. Results

### 2.1. Electrical Characteristics

A typical quasistatic current–voltage ( $I$ - $V$ ) curve of a Rh (3 nm)/YSZ (2.8 nm)/PCMO (20 nm)/SrRuO<sub>3</sub> (SRO, 30 nm)/SrTiO<sub>3</sub> (STO) layer stack is shown in **Figure 1a**. Bipolar resistive

switching is observed, where the device's resistance increases if a positive voltage sweep is applied to the top electrode. A reset process occurs switching the device from the LRS- to the HRS. Negative voltages, in turn, lead to a decrease in the device's resistance that corresponds to a transition from the HRS to the LRS, called the set process. Transitions between the resistive states occur gradually, enabling the device to be switched into intermediate resistance states: a property that could, in principle, allow usage as a multilevel memory device and is of particular interest for their implementation in neuromorphic circuits.<sup>[48]</sup> Neither a sharp set nor a sharp reset process occurs. Furthermore, no distinct electroforming step is required to initiate the device functionality, as this would typically result in a sudden drop in resistance during the initial cycle, which is not observed. However, for about one-third of the devices the first  $I$ - $V$  hysteresis loop deviates substantially from subsequent ones, as shown in **Figure 1b**. The maximum currents are higher during the first current–voltage sweep than afterwards. All further sweeps are typically smooth and very reproducible. In contrast, applying a negative voltage to the top electrode for the first sweep leads to a large decrease of the device resistance and to an irreversible ohmic behavior, hence to the failure of the device. Furthermore, we investigated device resistances as a function of device area, the results of which are shown in **Figure 1c**. The device resistance clearly scales inversely with the device area for both HRS and LRS. The gradients of linear fits, in a double logarithmic plot, to the data are close to the ideal value of  $-1$ . Because of the variability in the initial behavior as indicated above, the resistance scaling of the initial state deviates slightly from this ideal trend.

The current density is plotted as a function of the YSZ tunnel oxide layer thickness in a semilogarithmic scale in **Figure 1d**. A linear relationship is found for the three states—the initial, HRS, and LRS—indicating that a tunneling process governs the electrical transport through the device.

### 2.2. HAXPES

#### 2.2.1. Array-Type Samples

To investigate changes in the electronic structure of the active layers, namely, PCMO and YSZ, core-level HAXPES measurements were performed on the array-type sample, which is shown in **Figure 2a** and described in detail in the Experimental Section. The adoption of a grazing incidence geometry for the X-ray beam allows simultaneous probing of about 50 devices at once of the over thousand devices present in one stripe of devices on the sample. The device resistance states were programmed ex situ, in advance. The programming routine always started with a positive voltage sweep followed by three full voltage sweeps to the maximum positive and negative voltage. This was applied to remove the initial variations in the switching behavior that we described in Section 2.1. Thus, the HAXPES analysis averages over local fluctuations and defects related to the growth or fabrication procedures. The large probing depth of the emitted photoelectrons (about 10–12 nm) and the detection close to the surface normal provide sufficient sensitivity to the buried regions of interest.

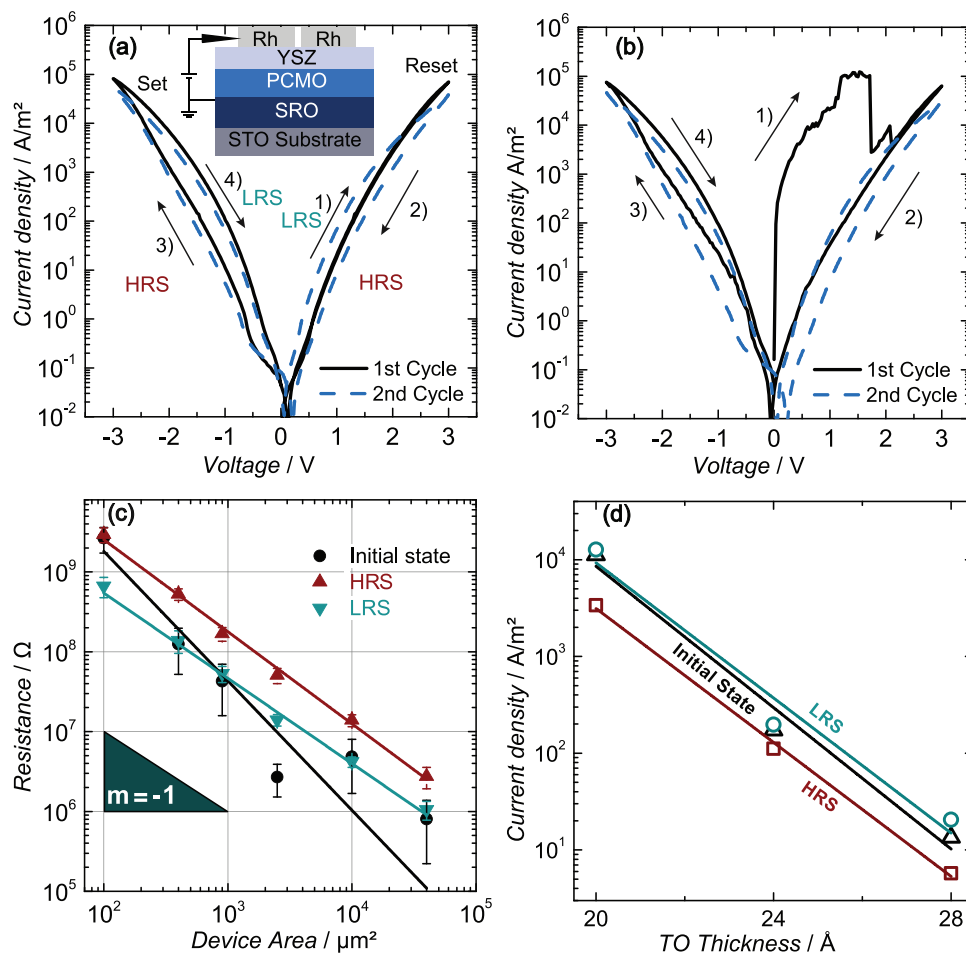


**Figure 1.** a) Quasistatic  $I$ - $V$  characteristic of a forming-free device with the layer sequence as shown in the inset. The voltage was applied to the top electrode. b) The  $I$ - $V$  characteristics of a device that showed higher currents during the initial  $I$ - $V$  cycle. c) The device currents in the HRS and LRS scale with the device area and d) depend exponentially on the thickness (20, 24, and 28 Å) of the YSZ layer, indicating a tunneling process.

The core-level spectra for the most representative elements of each layer, namely Mn 2p, O 1s, Rh 3d, and Zr 3d, are presented in Figure 2b–e. In order to minimize the measurement time and the related beam damage, we decided to record a single core-level spectrum for each layer, namely Rh 3d for the top electrode, Zr 3d for the YSZ layer, and Mn 2p for the PCMO layer, since Mn showed the most pronounced changes during electrical biasing in our previous HAXPES studies.<sup>[34]</sup> Each panel shows the spectra for arrays in the initial state (as prepared) and after programming to the HRS and LRS. No changes of the line shape or core-level shifts are evident in the spectra of Mn, O, or Rh, suggesting in particular the absence of significant changes in the chemical state of manganese for the PCMO layer. Similarly, the reproducibility of the line shapes indicates that the Rh remains metallic throughout switching and that no oxidation takes place.<sup>[49]</sup> The O 1s spectra actually show a minor variation in the shoulder at a binding energy (BE) of  $\approx 533$  eV for the HRS; however, the interpretation of this feature is not straightforward because the spectra also contain a contribution from the oxygen ions of the bare SRO present among the devices, as shown in Figure 1a. A comparison with the

O 1s spectrum for a bare SRO layer suggests that it is very likely that changes in the O 1s shoulder arise from slightly different spectral weights of this contribution in comparison to the active layers. Therefore, we do not draw any conclusions from the changes in the O 1s spectra. In contrast, clear changes can be observed in the Zr 3d core-levels shown in Figure 2e. The line shape is identical for the three states but we observed very consistent and reproducible shifts in binding energy, of the order of 0.1 eV. In particular, both the LRS and the HRS are shifted to lower BE compared to the initial state, with the HRS always shifted to slightly higher BEs than the LRS. We interpret this result as the build-up of an electrostatic charge within the YSZ rather than a change in the Zr oxidation state. Changes of the Zr valence state would require the appearance of secondary features with different binding energy, whereas in this case the Zr 3d spectrum remains unaltered in all states and shows only one doublet without any evidence for further components<sup>[50]</sup> within the detection level of the measurement. We propose that the electrostatic charge originates from  $O^{2-}$  ions, which migrate into the YSZ but are not charge-compensated by a valence change of the Zr ions.

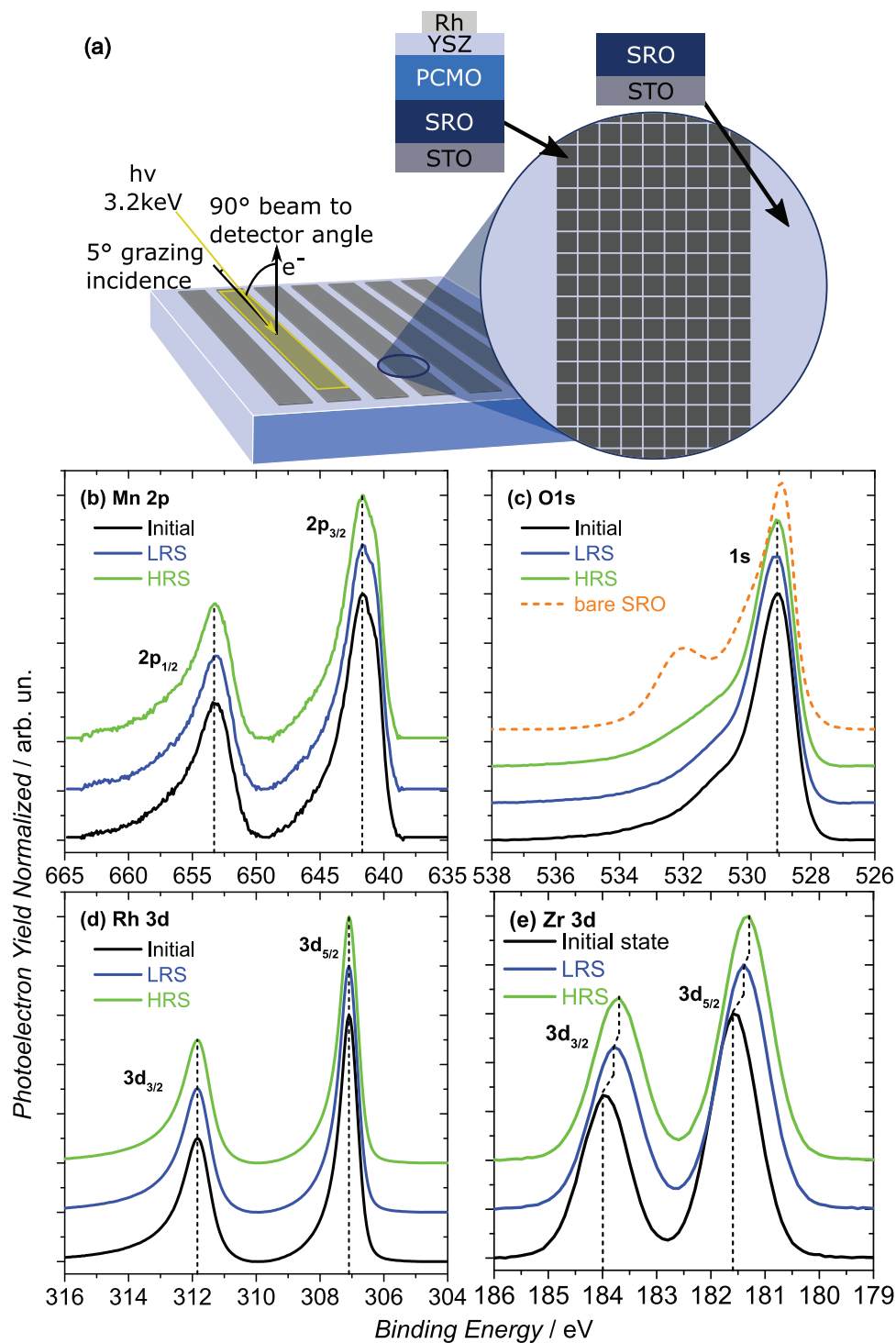


**Figure 2.** a) Core-level HAXPES spectra for arrays of devices with side length of 50  $\mu\text{m}$ . The panels show spectra for the core-levels of b) Mn 2p, c) O 1s, d) Rh 3d, and e) Zr 3d for the initial, high and low resistive states, respectively, with c) an additional O 1s spectrum for the bare SRO bottom electrode material. The photon energy was set to 3.2 keV. A Shirley background was subtracted from the data and they were normalized to the maximum intensity to allow for easier comparison of the line shapes and the peak positions.

### 2.2.2. In Operando Biased Devices

To confirm the observation of a Zr 3d core-level shift, we performed in operando HAXPES measurements on individual

devices. This way, the influence of device-to-device variations and alignment issues could be excluded since the same device was measured in different states and while a bias voltage was applied. We consider only the Zr 3d and the Rh 3d core-levels

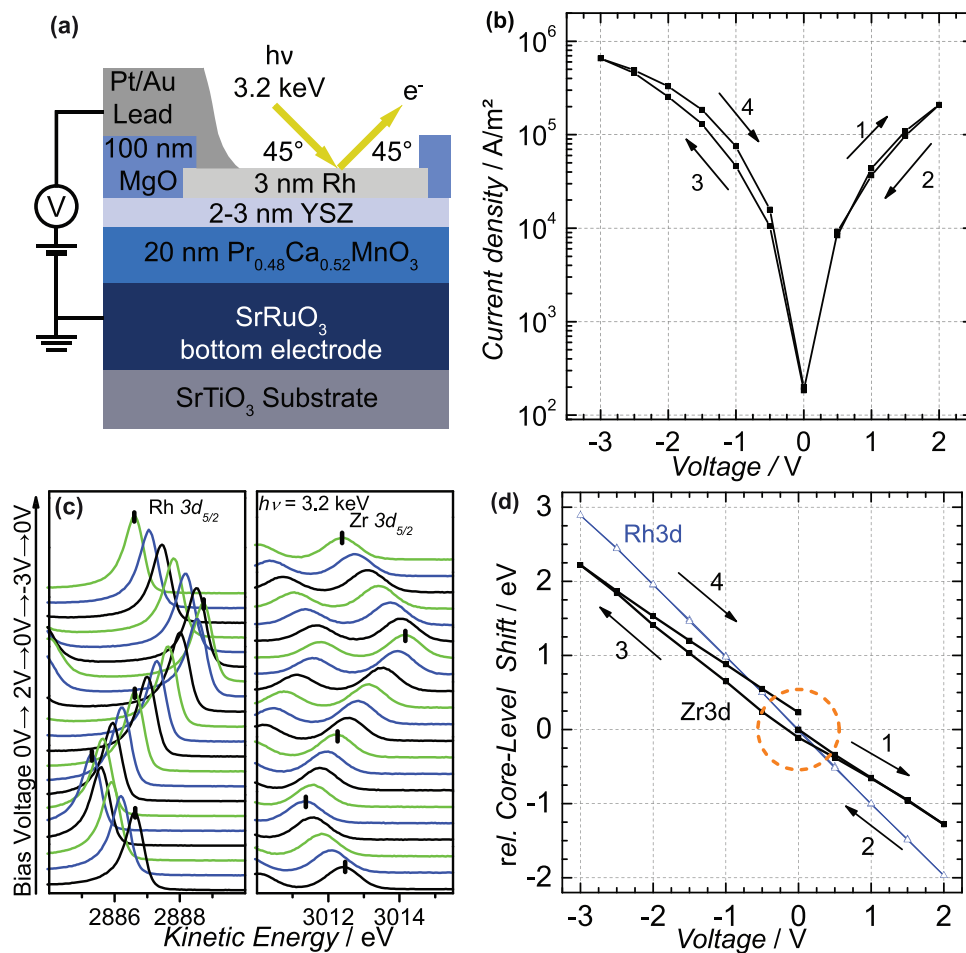


**Figure 3.** a) A schematic cross-section of the in operando type sample. b) The  $I$ - $V$  characteristics of a device measured in the UHV HAXPES chamber during collection of c) Rh  $3d_{5/2}$  and Zr  $3d_{5/2}$  spectra at the respective bias voltage. d) The resulting peak shifts in the Zr 3d and Rh 3d peak positions are shown relative to the initial position, before a bias voltage was applied. The orange circle highlights the remanent peak shifts at 0 V bias.

in this measurement because the O 1s core-level is a superposition of the contributions originating from YSZ, PCMO and to a large fraction the MgO insulator which surrounds the device and is therefore difficult to disentangle.

The resistively switching layer stack and the electrical setup are sketched in Figure 3a. More details are given in the Experimental Section. For the in operando measurements we applied bias voltages in the following sweeping direction  $0\text{ V} \rightarrow +2\text{ V} \rightarrow 0\text{ V} \rightarrow -3\text{ V} \rightarrow 0\text{ V}$  in increments of 0.5 V. During each voltage step we measured the Rh 3d and Zr 3d core-levels.

The  $I$ - $V$  curve of the device measured in the analysis chamber during X-ray exposure is shown in Figure 3b. Both vacuum as well as X-ray beam exposure result in an increase of the device current and in a shrinking of the hysteresis. This can be attributed to a loss of oxygen at the YSZ surface in vacuum which is significantly promoted by the presence of an X-ray beam as reported in the literature for a variety of oxide systems.<sup>[51–53]</sup> In our samples, the loss of oxygen will likely result in a reduction of the YSZ tunnel barrier height and thereby to an increase of the device current which might be more pronounced for the HRS, thereby resulting in a shrunk hysteresis. The experimental data and a more detailed

discussion are provided in Figures S3 and S4 in the Supporting Information.

However, despite of the increase of the device current, the general characteristics of the resistive switching are maintained, with a ratio between HRS and LRS of 2 at  $-1\text{ V}$  read-out voltage. The effects of biasing on the HAXPES spectra ( $h\nu = 3.2\text{ keV}$ ) are shown in Figure 3c where both the Rh 3d and Zr 3d core-level spectra consistently shift toward larger (smaller) kinetic energy for negative (positive) applied bias.

We evaluated the shifts in peak position relative to the unbiased state by fitting the Zr 3d and Rh 3d spectra with Voigt and modified Donjach–Sunjich curves, respectively.<sup>[54]</sup> As shown in Figure 3d, the Rh  $3d_{5/2}$  peak shift is linear with the voltage and does not show any hysteretic behavior. This linear shift is induced by the voltage drop at the ohmic contact to the metallic Rh layer. Hence, it provides a good reference for the observed Zr 3d core-level shifts. Interestingly, the Zr  $3d_{5/2}$  core-level exhibits a slight hysteresis. In particular, the relative shift increases in the negative direction during the voltage sweep from 0 to 2 V and returns during the negative voltage sweep from 0 to  $-3\text{ V}$ . Most importantly, at 0 V we observe a remanent relative shift of about 0.2 eV in the Zr 3d core-levels, which is



negative after the positive voltage sweep and positive after the negative sweep. This shift at zero bias confirms the shift of the Zr 3d core-levels detected for the ex situ measurements performed on the arrays shown in Figure 2e. The negative relative core-level shifts occurring at positive bias voltages correspond to a shift of the core-level toward lower binding energies. In turn, the positive relative core-level shift, occurring on the negative voltage branch, corresponds to a shift of the core-levels to higher binding energies. Photo carriers generated by the X-ray exposure might contribute to the changes observed in the  $I$ - $V$  curves under X-ray exposure shown in Figure S4 in the Supporting Information but should not affect the observed shift of the Zr 3d core-levels at 0 V after applying a switching voltage. Since the spectral line shapes detected for the whole sweeping cycle do not change, the observed shifts of the Zr 3d core-levels are consistent with the formation of a space charge in the YSZ layer rather than with the occurrence of redox reactions.<sup>[34]</sup>

### 2.3. Electron Microscopy

We complemented the HAXPES measurements with STEM-EELS to scrutinize local chemical variations in the device stacks. Figure 4 summarizes the EELS chemical analysis that

is common to all devices, irrespective of the resistive state. Figure 4a shows a section of a STEM image to indicate where the EELS data were collected. Figure 4b depicts a plot of the Mn, O, and Pr core-loss signals across the device's active layers, each normalized to their maximum value. The O signal appears relatively uniform across the PCMO layer, but drops substantially in the SRO layer in comparison to PCMO, and even beyond the drop expected from the change in O density between fully stoichiometric PCMO and SRO.

Figure 4c,d also shows evidence of a reduction of the Mn oxidation state at the YSZ/PCMO interface that suggests a migration of oxygen from the PCMO into the YSZ, similar to previous observations of the Ti/PCMO system.<sup>[35]</sup> Figure 4d plots normalized Mn  $L_{2,3}$  EELS edges collected from the middle of the PCMO layer (full line) and just under the YSZ/PCMO interface (dashed line). Clear peak shifts and a simultaneous change in the relative intensities of the  $L_2$  and  $L_3$  peaks were observed at the YSZ/PCMO interfaces of all devices and are consistent with previous observations of chemical reduction.<sup>[22]</sup> The magnitude of the peak shift at the YSZ/PCMO interface is plotted in Figure 4c relative to the bulk value of the middle of the film. It indicates an up to  $-1.5$  eV shift, gradually diminishing across 12 nm to the bulk value, which is consistent<sup>[22,55]</sup> with an oxidation state change from an

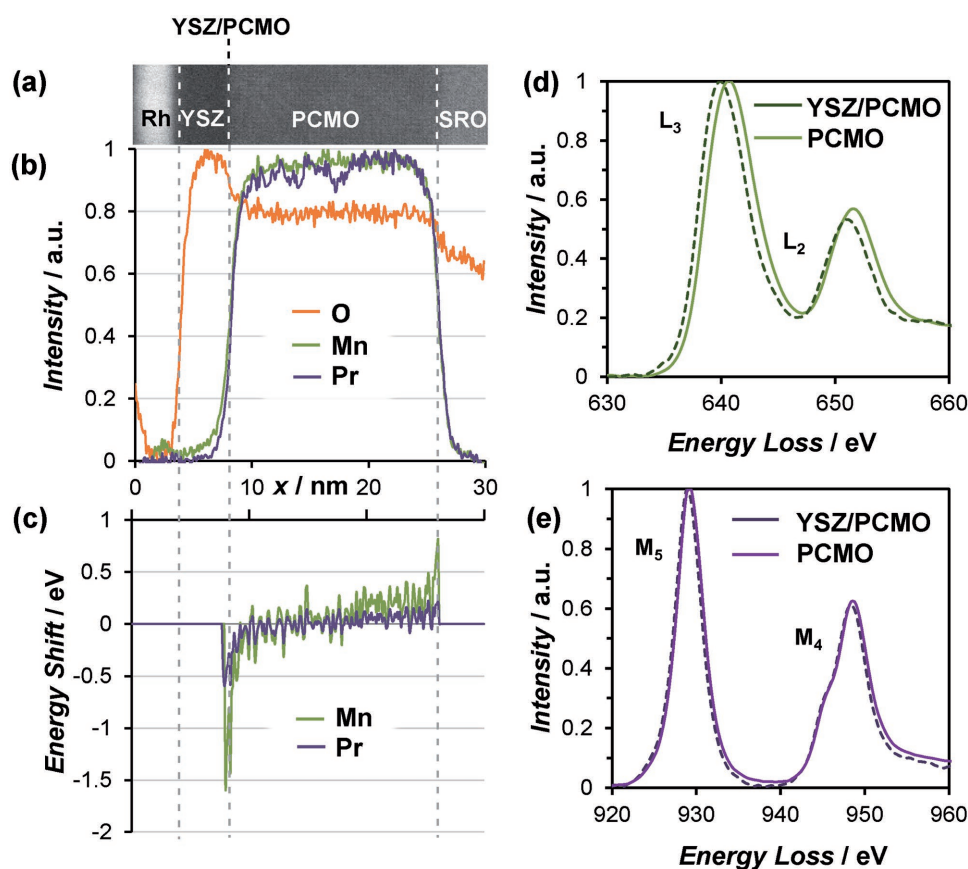


**Figure 4.** Summarized EELS analysis of a typical device showing: a) dark field STEM image of the layer sequence; b) normalized elemental composition through the stack determined from processed O K, Mn  $L_{2,3}$  and Pr  $M_{4,5}$  EELS edges; c) variations in the Mn  $L_{2,3}$  and Pr  $M_{4,5}$  peak positions as a function of position throughout the layers (note the alignment with the image in (a)); d) typical Mn  $L_{2,3}$  EELS and e) Pr  $M_{4,5}$  edges collected from the middle of the PCMO layer and at the interface with the YSZ.

average interfacial value of  $\text{Mn}^{2.7+}$  to the bulk value of  $\text{Mn}^{3.5+}$ . The spatial extent of the chemical reduction does vary from device to device, which perhaps indicates a degree of inhomogeneity that could underpin the initial variation in electrical behavior of the devices described above. Similarly, the Pr  $M_{4,5}$  EELS edges plotted in Figure 4e show less variation across the device, but with a small  $\approx 0.5$  eV shift within a few nanometers of the interface that, as with the Mn, is consistent with interfacial reduction. Throughout the device, the Pr  $M_4$  peak shows a weak shoulder at an energy loss of approximately 945 eV that, in comparison with previous EELS<sup>[56]</sup> and XAS<sup>[57,58]</sup> studies, is consistent with the presence of a notable fraction of  $\text{Pr}^{3+}$ . There are few previous quantitative EELS studies of the Pr  $M_{4,5}$  edges for comparison, but a previous XAS study<sup>[58]</sup> indicated a peak shift of 1.7 eV between  $\text{Pr}^{3+}$  and  $\text{Pr}^{4+}$  states, suggesting that the interfacial shift of 0.5 eV observed here could represent a reduction and change of oxidation state of up to 0.3 units within a few nanometers of the interface. However, absolute determination of the Pr oxidation state would require further comparisons with standard reference materials, which we have not attempted here.

Turning now to a comparison of switched devices, it is important to note that electrostatic effects will not affect EELS spectra in the same manner as HAXPES spectra, where core-level shifts are observed. Instead, it would be anticipated that

the migration of small quantities of oxygen anions would affect minor changes in the oxidation state of counterions and in the local bonding environments discerned in the EELS fine structure.

Subtle spatial inhomogeneities in the PCMO chemistry dominate the EELS comparisons of HRS and LRS data sets rather than unambiguous signatures of the devices' switched state. Figure 5 summarizes the typical (a) Mn  $L_{2,3}$  and (b) Pr  $M_{4,5}$  EELS edges collected from the YSZ/PCMO interface of (blue) LRS and (red) HRS devices. In the case of the Mn data, two distinct data sets are plotted (full and dashed colored lines) for each device, taken from different locations along the YSZ/PCMO interface. They are illustrative of the typical chemical variations observed. Although there was no discernible structural variation in STEM imaging, the Mn  $L_{2,3}$  peak position and intensity ratio vary across the interface. Using the same analysis of the oxidation state used elsewhere,<sup>[55]</sup> we estimate the Mn oxidation state at the YSZ/PCMO interface to vary between 2.2 and 3.5. Small-scale, local variations of this nature would be inaccessible to HAXPES analysis. However, there is no clear correlation between electrical resistance state and interfacial Mn oxidation state.

Curiously, more reproducible changes are observed in the Pr interfacial oxidation state throughout the device, as summarized in Figure 5b. Both HRS and LRS data sets show the

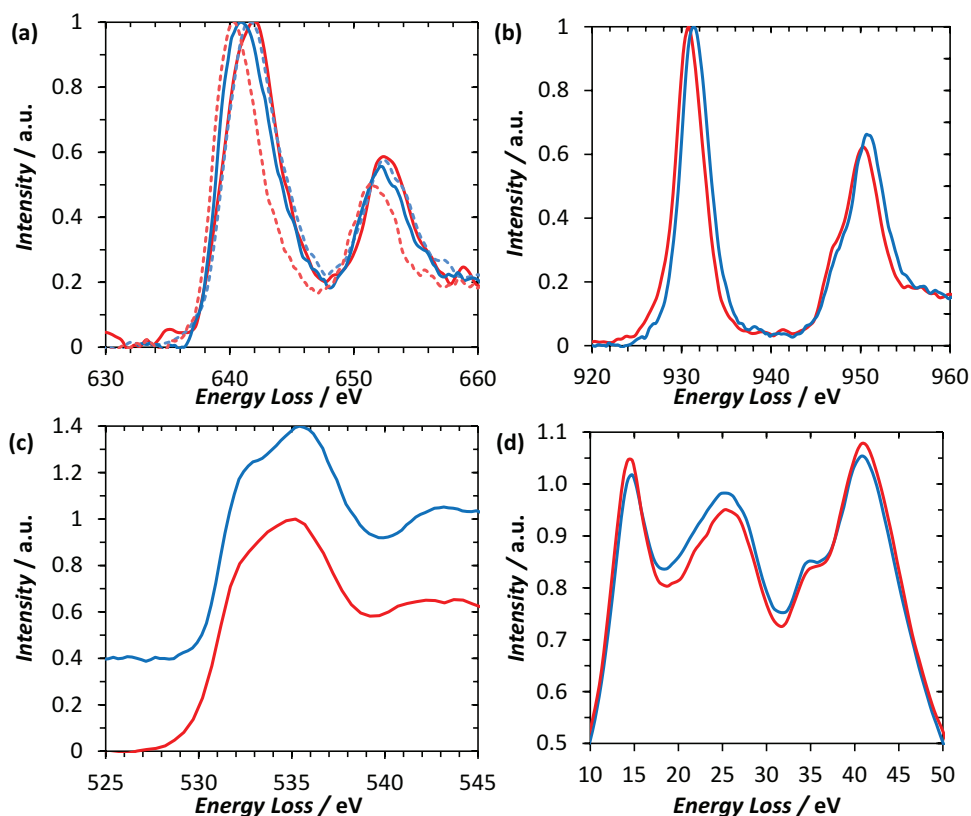


**Figure 5.** Typical a) interfacial Mn  $L_{2,3}$  and b) bulk Pr  $M_{4,5}$  edges for LRS- (blue) and HRS- (red) set devices at the YSZ/PCMO interface, with (a) additional dashed lines collected at a different position and therefore indicating spatial inhomogeneities. While the Pr shows systematic variations in peak position, there is variability in the form of the Mn peaks, indicating inhomogeneous variations in the Mn oxidation state. c) O EELS K-edge and d) low-loss EELS show details of typical data for HRS (red) and LRS (blue) devices. The trends shown are indicative of the majority of locations measured for each device although (see text) spatial variations are evident in each case.

$M_4$  shoulder at 945 eV that indicates the presence of  $\text{Pr}^{3+}$  and the shoulder is more pronounced for the HRS. There is also a consistent shift of the Pr peak positions toward lower energies in the HRS device, of up to 0.5 eV, again indicating reduction of order 0.3 units. (As indicated above, there are insufficient quantitative EELS analyses of the Pr  $M^{4,5}$  edges to provide an absolute, rather than relative, measure of oxidation state.) In addition, the  $M_4:M_5$  integrated peak ratio increases, which all together clearly indicate a reduction of the Pr. Such a change is less commonly seen in the A-site of perovskites, as it is typically the B-site (Mn here) that compensates for oxygen vacancies through chemical reduction because it is directly bonded to the oxygen ligands. However, Pr is well known to form stable compounds of both  $\text{Pr}^{3+}$  and  $\text{Pr}^{4+}$  and variations in A-site oxidation state have been observed recently in the related  $\text{Pr}_{0.5}\text{Ca}_{0.5}\text{CoO}_3$ ,<sup>[57–59]</sup> system so it is plausible that similar variations in the Pr oxidation state occur here. Thus, charge balancing upon oxygen migration appears to be split between Pr and Mn sites. It is important to note that the observed Pr reduction in the HRS is consistent with the migration of oxygen from the PCMO to the YSZ during positive biasing of the top electrode.

Moreover, subtle, switching-dependent variations in EELS are observed in both the YSZ's O-K edge data and in the low-loss spectra, which is expected for a mechanism based on O migration leading to changes in properties of the tunnel barrier. Figure 5c displays the core-loss oxygen K edge, where the LRS data sets have been separated vertically for clarity. Although only a subtle change, there is a consistent difference between the LRS and the HRS in the shape of the main K edge peak, which appears more rounded for the HRS. Even in crystalline systems, the form of the oxygen K edge of zirconia is complicated by the number of distinct bonding environments experienced by oxygen atoms in the relaxed unit cell. An inclusion of anion vacancies induced by Y doping further increases the number of distinct environments, and the excitation of O in each unique bonding environment will contribute a multiplet of components to the measured spectrum.<sup>[60,61]</sup> For example, the pre-edge shoulder has been used to distinguish tetragonal and cubic (crystalline) YSZ,<sup>[60]</sup> the latter of which has a less prominent shoulder and would be more consistent with the LRS spectrum of Figure 5c. A structural change from tetragonal to cubic YSZ has also been linked to changes in the oxygen vacancy concentration.<sup>[62]</sup> It is suggested<sup>[63]</sup> that the electronic and structural properties of stabilized zirconia can be controlled by the structural disorder around the oxygen vacancies, which could affect the electrical properties of the tunnel barrier. The YSZ in the samples investigated here is largely amorphous (see Figure S5, Supporting Information) and the changes observed here may therefore be indicative of slight changes to the local bonding environment within the YSZ tunnel barrier upon switching. We propose that these changes derive from the migration of oxygen anions into the vacancy sites induced by Y doping and would be discernable even if the absolute concentration of additional anions is low.

The low-loss spectra extracted from YSZ shown in Figure 5d also exhibit switching-dependent features. The spectra are in good agreement with those published in the literature.<sup>[60–62,64]</sup> Features below  $\approx 22$  eV are ascribed to interband transitions from the O 2p state to empty Zr states; the broad peak around

26 eV is a plasmonic excitation; and features above 30 eV correspond to the Zr  $N_{2,3}$  edge, i.e., interband transitions from the Zr 4p state to other unoccupied Zr states.<sup>[65]</sup> One might therefore expect the greatest changes upon switching to be observed below 30 eV, which is observed here. There is variability in the intensity of the peak at 15 eV across all data sets but the LRS data sets tend to have a more pronounced plasmon peak that would be consistent with an increased metallic character of the YSZ. Some regions of LRS devices yield spectra that barely differ from the typical HRS spectrum in the region of the plasmon, once again suggesting the presence of chemical inhomogeneities that could not be observed in the HAXPES analysis.

### 3. Discussion

#### 3.1. Initial Behavior

Figure 6 provides a schematic overview of device operation. In contrast to the LRS and the HRS, the initial state resistance shows a deviation from the area scaling law, which is a significant characteristic of an interface-type resistance switching mechanism. This deviation vanished after an initial voltages sweep with positive polarity applied to the top electrode. Applying a negative voltage for the initial cycle, leads to a large decrease of the device resistance and to an irreversible breakdown of the device.

The HAXPES measurements did not reveal any significant differences in terms of line shape or chemical shifts for Rh 3d, O 1s and Mn 2p core-levels between initial state and the switched states. However, in the EELS measurements, which are much more sensitive to spatial variations in chemical properties, we found a slight reduction of PCMO at the interface of YSZ. In particular, PCMO exhibited a Mn oxidation state of 2.7 at the YSZ interface whereas it increased deeper in the PCMO film to 3.5, which corresponds to the mixed valence state for PCMO of our nominal target stoichiometry (see Figure 6a). This was common to all devices, irrespective of their resistive state. One can therefore conclude that the YSZ film draws oxygen from the PCMO layer during its deposition, similar to the situation in the Ti/PCMO system<sup>[35]</sup> or for YSZ grown on  $\text{SrTiO}_3$  single crystals.<sup>[66]</sup> For the switched devices, both the HRS and the LRS exhibit a further reduction of the Mn oxidation state, down to 2.2 (see Figure 6b), but with notable inhomogeneity along the YSZ/PCMO interface. This manganese reduction can be attributed to a locally varying oxygen depletion of the PCMO near the YSZ. Combining these indications, one might speculate that the as-deposited YSZ is not fully oxidized, perhaps because kinetic limitations during growth at room temperature limit the diffusion of oxygen from the PCMO required to form a homogenous fully oxidized layer. This oxidation then occurs by migration of oxygen ions when applying a positive bias voltage for the first time, with devices performing more uniformly thereafter (see sketch in Figure 6a,b). Thus, the initial inhomogeneities at the YSZ/PCMO interface could account for the device-to-device variability in the first voltage sweep. Conversely, if applying a negative bias voltage for the first  $I-V$  sweep, the device breaks



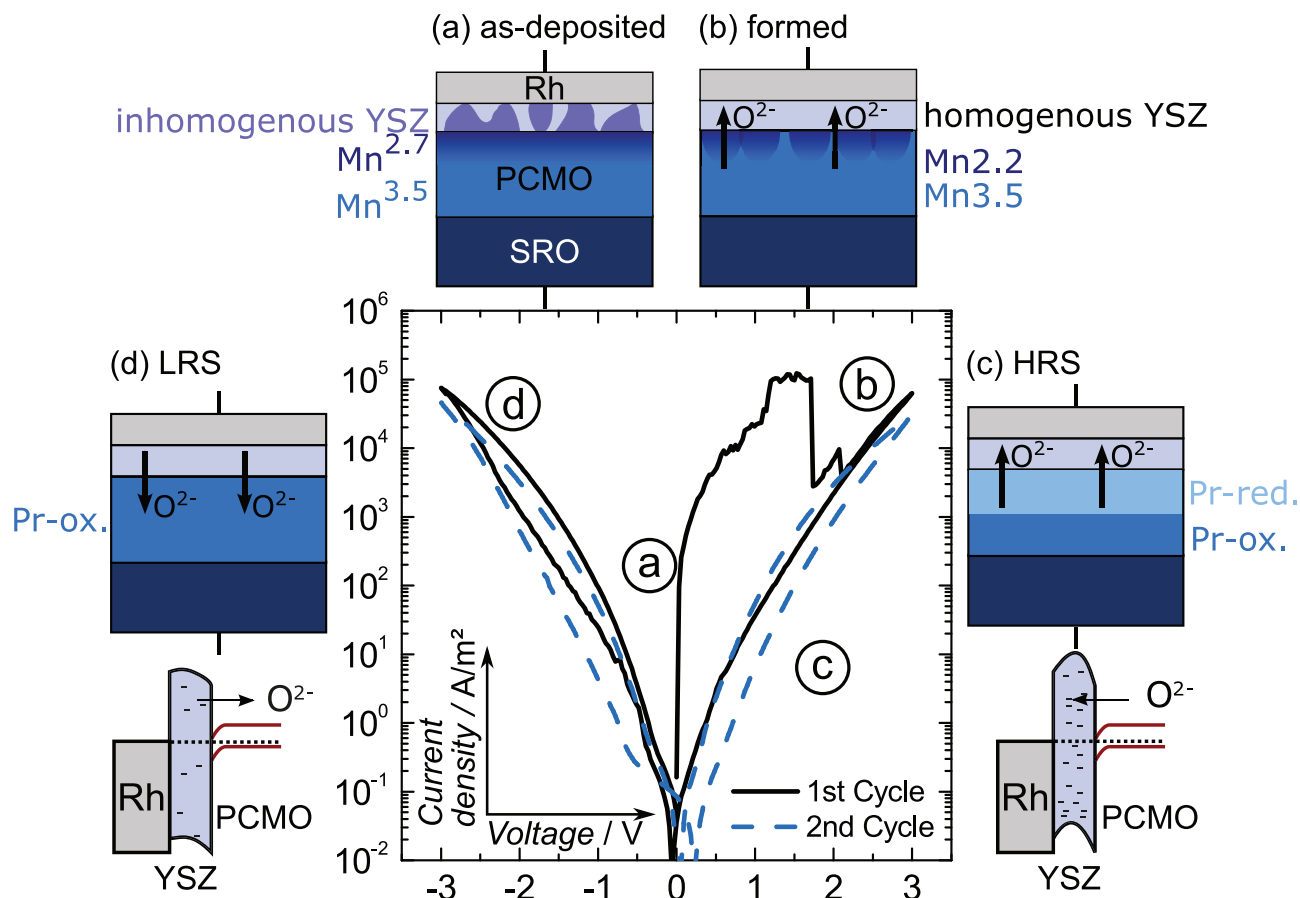


**Figure 6.** Schematic summary of the electrical characteristics and the spectroscopic results in which we distinguish the initial behavior indicated by (a) and (b) and the reproducible resistive switching indicated by (c) and (d). a) In the as-deposited state YSZ is inhomogeneous and not fully oxidized but has drawn oxygen from PCMO at the interface. b) During the first positive voltage sweep, more oxygen ions move from PCMO to YSZ, and very likely homogenize the YSZ, which causes a kind of forming step and the resistances of the device increases. After the initial full sweep, the resistive switching is fully engaged. Positive voltages RESET the device to the HRS c) which is characterized by a negative space charge in the YSZ, causing the effective barrier height to increase, and reduced Pr in the PCMO. This originates from oxygen ions which migrated into the YSZ layer. d) Reversing the bias voltage depletes the YSZ from excess oxygen ions, hence reducing the space charge and the effective tunnel barrier height. PCMO gets more oxidized, indicated again by the oxidation state of Pr.

down because the initially more conductive regions of the YSZ get even more conductive as oxygen ions migrate into the PCMO, leading to an irreversible electrical breakdown within the YSZ layer.

It is to be expected that oxygen migration will affect the conduction characteristics of both the YSZ and the PCMO layer. To confirm whether changes in the YSZ or in the PCMO dominate the overall transport properties, we applied a simplified transport model to the current–voltage characteristics of our devices. The model is a series connection of an ohmic resistance, representing the SRO and other ohmic losses, and a field-accelerated polaron hopping model<sup>[67]</sup> that describes the current transport in the PCMO layer. (Further details of the model are described in the Supporting Information, with details of the applied parameters to be found in the Experimental Section.)

Figure 7a shows in blue colors the measured read-out  $I$ – $V$  sweeps for devices with different YSZ thicknesses. The green trace shows the modeled  $I$ – $V$  curve originating from polaron hopping transport within an oxygen-depleted PCMO interface layer. We find that the currents that would arise if only either

the PCMO or the series resistances were present significantly exceed the currents actually measured. In order to describe the current by the polaron hopping mechanism, physically unrealistic parameters for the hopping barrier would be necessary. By adding another element in series to describe the YSZ tunnel barrier, however, we were able to achieve good fits to the  $I$ – $V$  curves of the HRS and the LRS, as shown in Figure 7b. In particular, we used a tunnel barrier with different electrode materials on either side, as suggested by Simmons,<sup>[68]</sup> resulting in Equation (S1) in the Supporting Information. In our case this corresponds to the YSZ tunnel barrier with Rh on top and PCMO below. The barrier heights used for the LRS were  $\phi_1 = 1.3$  eV and  $\phi_2 = 1.4$  eV and for the HRS  $\phi_1 = 1.4$  eV and  $\phi_2 = 1.5$  eV, respectively.

Although a more elaborate model is needed to describe this device more accurately, we conclude that the electrical transport is dominated by the YSZ tunnel barrier. The influence of the PCMO layer in defining the electrical transport can be neglected. This is supported by the strong exponential increase of the current with YSZ thickness that was shown in Figure 1d. Thus, we propose that the reduced, less conductive

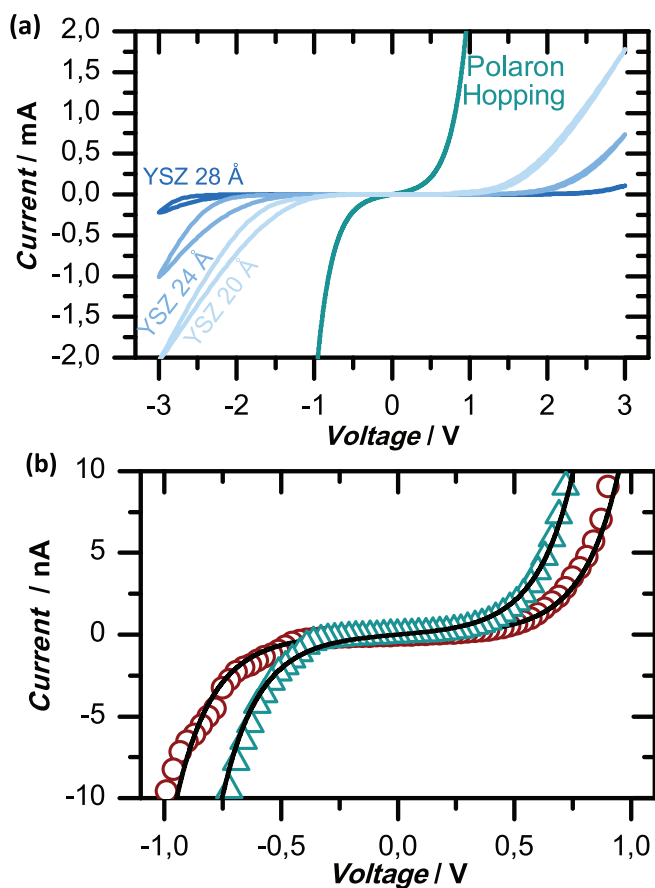


**Figure 7.** (a)  $I$ - $V$  curves for 20, 24, 28 Å thickness of the YSZ in comparison with  $I$ - $V$  curves which result from the model if only the polaron hopping conduction or the series resistance was present. (b) Read-out  $I$ - $V$  sweeps from  $-1$  to  $1$  V, for a device with  $50 \times 50 \mu\text{m}^2$  edge length and an YSZ layer with a thickness of 2.8 nm, for the HRS (red circles) and LRS (green triangles). The full lines are fits with a model based on a series connection of a Simmons-tunnel barrier, polaron hopping conduction. The exact parameters used can be found in the text and the experimental information.

regions of PCMO do not influence the overall resistance of the device as long as the YSZ layer acts as tunnel barrier. Similarly, we can exclude the variations in the manganese oxidation state observed along the YSZ/PCMO interface as being critical to the variability of as-deposited devices. Instead, the inhomogeneities in the YSZ, which are evened out by the migration of oxygen ions during the initial positive voltage sweep, dominate the initial device variability, as sketched in Figure 7b.

### 3.2. Switching Model

Our electrical measurements, which showed a gradual increase in device resistance for positive bias voltages, and also a gradual decrease in device resistance at negative voltages, can be explained by a model that is based on the movement of a relatively small concentration of oxygen ions and the resulting electrostatic charging of the YSZ barrier. Oxygen ions move into the YSZ layer upon application of a positive bias to the top electrode, leading to an increase of the tunnel barrier height and hence to a decreased tunnel current in the HRS state, as

sketched in Figure 6c. Conversely, applying a negative bias would lead to the LRS state by removing oxygen ions from the YSZ as shown in Figure 6d. This modulation of the effective tunnel barrier height is caused by an excess negative charge that accumulates and depletes in the YSZ by the migration of oxygen ions.<sup>[36]</sup> Because the current densities are low, and as the area dependence suggests uniform switching, we can neglect Joule-heating and heat-assisted oxygen movement in describing our devices. The migration has to be attributed to a significant reduction of a potential barrier by the electric field, leading to an exponential increase in successful jump events of the oxygen ions even at room temperature.<sup>[36]</sup>

The existence of an electrostatic tunnel barrier is confirmed by the chemical shifts in the PES spectra, which are not accompanied by the spectral changes that would arise from oxidation state changes and which can only be attributed to a static space charge in the YSZ layer. Negative charges increase the kinetic energy of the photoelectrons and hence shift the spectrum toward lower binding energies; conversely, a more positive charge decreases the kinetic energy of the photoelectrons and the spectrum shifts toward higher binding energies. In comparison to the initial state, we found consistent shifts toward lower binding energies for both the LRS and the HRS for the ex situ switched array-type samples as well as for the in situ switched device. This direction is consistent with oxygen migration into the YSZ during a positive bias voltage, leading to a barrier region with negative space charge. Upon inversion of the voltage, the oxygen migrates back into the PCMO and the negative space charge reduces again. This reduction results in a remanent peak shift compared to the initial position for the array-type sample, as can be seen in Figure 3d. This model of a reversible movement between the YSZ and the PCMO layer is substantiated by our EELS data which confirm a change of the oxygen content in the YSZ layer (Figure 5c) and a simultaneous reduction of the Pr valence in the HRS (Figure 5b).

Based on the local changes of the electronic structure of PCMO detected by our EELS analysis we have to keep in mind that the electronic structure of the PCMO as well as the band bending at the PCMO interface changes during electrical biasing, as suggested by Sawa and co-workers for PCMO/TiO<sub>2</sub>/Ti devices.<sup>[22]</sup> However, based on our HAXPES analysis, we consider the space charge formation in the YSZ to be the dominant effect and propose the simplified band diagram shown in Figure 6c,d, in which the HRS is described by a more negatively charged YSZ layer than the LRS. This model slightly differs from the one suggested in ref. [36] since we have no positively charged region, only a less negatively charged YSZ barrier in the LRS. A less negatively charged YSZ layer should result in a decrease of the effective barrier height for the LRS, which the Simmons fit indicates to be about 0.2 eV. Although the exact impact of the electrostatic charging of the YSZ tunnel barrier would require elaborate ab initio calculations, this simple model already confirms that the extent of the change in the resistance of the device is consistent with a change in the mean height of the tunnel barrier.

One should keep in mind that the electrostatic shifts in the Zr 3d core-level could also be explained by the injection of electrons into the YSZ barrier and do not necessarily prove ionic

motion. It is also important to note that substantial electrostatic changes can arise from the migration of relatively small quantities of charge. In this regard our EELS provides two different kinds of indication for oxygen ion movement. The most important one is the observed change in the O-K edge between HRS and LRS, which we assign to structural changes in the YSZ induced by changes in the oxygen vacancy concentration,<sup>[62]</sup> in agreement with the subtle variations in the low-loss EELS spectra. Furthermore, the observed reduction of the Pr valence state detected by EELS analysis suggest a slight reduction of the PCMO at the YSZ interface in the HRS. This reduction of PCMO and the increase in the oxygen vacancy concentration in the YSZ occur simultaneously when switching the device to the HRS. This is a strong indication that oxygen is exchanged between YSZ and PCMO during resistive switching.

#### 4. Conclusion

We have investigated in detail nonfilamentary, resistively switching SRO/PCMO/YSZ/Rh heterostructures by HAXPES and STEM-EELS analysis and have compared the result to the electrical properties of the devices. In combination with in operando HAXPES measurements, our data provide conclusive experimental evidence that electrostatic charging of the YSZ takes place, caused by the exchange of oxygen ions between the YSZ tunnel barrier and the PCMO layer. Although STEM-EELS analysis indicated lateral inhomogeneities in the PCMO layer, a key advantage of this device type is that the resistive states are unaffected by such stochastic variations since the current transport is solely determined by electron tunneling across the YSZ barrier. This type of resistive switching system is therefore insensitive to stochastic redox and thermal processes, unlike many filamentary-type resistively switching systems. It is instead governed by the properties of a deliberately deposited tunnel barrier, whose properties can be tailored according to technological requirements.

#### 5. Experimental Section

The layer stack that is a common part of all samples was grown by Pulsed Laser Deposition. SrTiO<sub>3</sub> (STO) (001) single crystals were TiO<sub>2</sub>-terminated by a buffered HF solution and annealed at 950 °C or 2 h. First, 30 nm of SrRuO<sub>3</sub> ( $T = 650$  °C,  $p_{O_2} = 0.133$  mbar,  $1.2$  J cm<sup>-2</sup>, 2 Hz) were grown as a bottom electrode. Subsequently, 20 nm of Pr<sub>0.48</sub>Ca<sub>0.52</sub>MnO<sub>3</sub> (PCMO) ( $T = 700$  °C,  $p_{O_2} = 0.133$  mbar,  $3.1$  J cm<sup>-2</sup>, 5 Hz) and 2.8 nm of YSZ ( $T =$  room temperature,  $p_{O_2} = 1 \times 10^{-4}$  mbar,  $1.7$  J cm<sup>-2</sup>, 5 Hz) were grown in situ. SRO and PCMO grow in an epitaxial manner while YSZ deposited at room temperature does not. After breaking the vacuum for the first time, a top electrode consisting of 3 nm Rh was then deposited by electron beam evaporation. We used Rh as top electrode because it is a much weaker absorber for photoelectrons than classical inert top electrodes such as Au and Pt because of its smaller atomic weight. Rh is chemically similar to Au and Pt and our measurements show identical  $I$ - $V$  characteristics for Rh and Pt electrodes. We have successfully employed Rh in our previous studies on SrTiO<sub>3</sub> devices.<sup>[69]</sup>

The in operando type of samples incorporated Pt/Au leads, which were again deposited by e-beam evaporation and electrically isolated using an additional MgO insulation layer that was grown by PLD using the same conditions as for YSZ.

Based on this layer sequence, different kinds of sample were prepared. To investigate the device current dependence on the device area, square devices were patterned with side length of 10, 20, 30, 50, 100, and 200 μm. The second kind of sample was used for experiments in which the devices were set ex situ to a certain resistive state. They consisted of single devices  $50 \times 50$  μm<sup>2</sup> in size and arranged in arrays about 7 mm long and 0.5 mm wide. The spacing between the electrodes was about 10 μm and the patterning was done by photolithography and dry etching.

Samples for the in operando biasing experiments were prepared in accordance with the technological requirements for electrically addressing samples in the HAXPES ultrahigh vacuum chamber that is available at the GALAXIES beamline of the SOLEIL synchrotron. The specific sample holder is shown in the Supporting Information. It provides two electrical contacts to the outside, so the samples had to be designed in a way that individual devices could be electrically contacted to the contacts of the sample holder. Therefore, devices were patterned to a size of  $200 \times 50$  μm<sup>2</sup> size and a MgO insulating layer was then deposited around the devices and metallic Pt/Au leads were deposited to enable the devices to be electrically addressed individually while inside the HAXPES chamber. The Au/Pt leads as well as the SRO bottom electrode were connected to the sample holder's electrical contacts by wire bonding.

The ex situ array samples were programmed by voltage sweeps at  $1$  V s<sup>-1</sup> to HRS (3 V) and LRS (-2 V) using a semiautomatic probe station (PA200 from Süss MicroTec) and an Agilent Technologies B1500A Semiconductor Device Parameter Analyzer. Every programming step was preceded by a positive voltage sweep to eliminate possible sample-to-sample deviations occurring during the initial sweep. A Keithley 2611 source meter was used to address the devices electrically in situ, grounding the bottom (SRO) electrode and using the top electrode as the source contact. We performed the 0 V measurements while connecting the cables with a 50 Ω resistor in order to provide well defined experimental conditions. Preliminary experiments showed that the resistive switching under HV conditions does not differ compared to resistive switching under ambient conditions, which is shown in the Supporting Information.

The HAXPES measurements were performed at the GALAXIES beamline of the French synchrotron radiation facility SOLEIL. In all cases, a photon energy of 3200 eV was used as a compromise between maximizing the depth from which information could be obtained while minimizing the reduction in X-ray absorption cross-section that occurs with increasing photon energy. All the measurements were performed at room temperature, with an overall energy resolution of about 0.4 eV. The array-type sample allowed a grazing angle of 5° to be used that maximizes the bulk intensity. An angle of incidence of 45° from the sample normal was chosen for the in operando type devices to match the size of the beam footprint to the device size and also to maximize the PES signal from the buried YSZ and PCMO. More details are reported in the Supporting Information. The probing depth was estimated on the basis of the depth-dependent exponential decay of the emitted electron intensity, regulated by the electron attenuation length (EAL).<sup>[70]</sup> As the detection geometry of the photoelectrons was very close to the normal to the surface of the devices, the EAL can be directly evaluated from the material-dependent inelastic mean-free path (IMFP) provided by the NIST Electron IMFP Database (<https://www.nist.gov/srd/nist-standard-reference-database-71>). To estimate which fractions of the stack we are actually probing, the specific case of the Mn 2p spectrum can be considered. The kinetic energy of the Mn 2p photoelectrons is around 2500 eV, thus leading to the IMFP value of 3.5 nm. The corresponding probing depth is 10.5 nm, subtracting the thickness of Rh and YSZ we actually probe  $10.5$  nm -  $5.8$  nm =  $4.7$  nm of PCMO, corresponding to about 25% of the whole PCMO film. Hence, we are probing mostly the YSZ/PCMO interface region rather than the whole PCMO film and the first nm of PCMO at the interface contributes for about 33% to the whole Mn 2p spectrum.

Cross-sectional samples for electron microscopy analysis were prepared using standard protocols on an FEI Nova DualBeam Focused

Ion Beam instrument, selecting material from the center of devices and ion-milling it to typically 50–100 nm thickness. Samples were typically prepared and analyzed within 48 h of electrical characterization. Electron microscopy was then performed on a JEOL ARM instrument that is equipped with a cold field emission gun and operated at 200 kV. Data were acquired in STEM mode. A Gatan Quantum spectrometer was used for EELS and incorporated hardware and software for DualEELS<sup>[71]</sup> and Spectrum Imaging<sup>[72]</sup> methodologies, both of which were used to map chemical variations across the devices. EELS data sets were prepared using standard deconvolution and background subtraction algorithms within the Gatan Digital Micrograph software package.

The following parameters were chosen for the modeling of the transport mechanisms. For the polaron hopping, room temperature and a polaron hopping distance of  $a = 4 \text{ \AA}$  was assumed, the latter according to the Mn–Mn distance. The device size was  $A = (50 \text{ \mu m})^2$  and the polaron density  $n = 1 \text{ nm}^{-3}$ . As in preceding works published in ref. [35], a thickness of the oxygen depleted region in the PCMO of  $r = 1.6 \text{ nm}$  and an activation energy for hopping  $\Delta E = 0.4 \text{ eV}$  was used. The thickness of the tunnel barrier was  $d = 2.8 \text{ nm}$ . Based on the phonon frequency an attempt rate for hopping of  $\omega = 10^{13} \text{ Hz}$  was used. An effective mass  $m$  of  $1.19m_e$  was used for the Simmons tunnel barrier. This value for the effective mass was obtained by the fit and it was held constant in the different states in order to minimize the number of variables in the fit.

## Supporting Information

Supporting Information is available from the Wiley Online Library or from the author.

## Acknowledgements

The HAXPES analysis was performed at the GALAXIES beamline at SOLEIL under the proposal 20140991. The authors thank the beamline staff Jean-Pascal Rueff and Denis Ceolin for their support and C. Bäumer for helpful discussions. Funding from the DFG (German Science Foundation) within the collaborative research center SFB 917 “Nanoswitches” is gratefully acknowledged. RD also acknowledges funding from the W2/W3 program of the Helmholtz association. DAM, PP and MF are grateful to the Engineering and Physical Sciences Research Council of the UK for funding through grants EP/I00419X/1 and EP/M506539/1. Electron microscopy data collected during these grants for this paper are available at <http://dx.doi.org/10.5525/gla.researchdata.458>.

## Conflict of Interest

The authors declare no conflict of interest.

## Keywords

HAXPES, PCMO, resistive switching, STEM-EELS, tunnel ReRAM

Received: April 28, 2017

Revised: August 24, 2017

Published online: October 10, 2017

[1] R. Waser, R. Dittmann, G. Staikov, K. Szot, *Adv. Mater.* **2009**, *21*, 2632.

[2] A. Beck, J. G. Bednorz, C. Gerber, C. Rossel, D. Widmer, *Appl. Phys. Lett.* **2000**, *77*, 139.

- [3] P. Parreira, G. W. Paterson, S. McVitie, D. A. MacLaren, *J. Phys. D Appl. Phys.* **2016**, *49*, 95111/1.
- [4] Y. Watanabe, J. G. Bednorz, A. Bietsch, C. Gerber, D. Widmer, A. Beck, S. J. Wind, *Appl. Phys. Lett.* **2001**, *78*, 3738.
- [5] A. Asamitsu, Y. Tomioka, H. Kuwahara, Y. Tokura, *Nature* **1997**, *388*, 50.
- [6] H. Oshima, K. Miyano, Y. Konishi, M. Kawasaki, Y. Tokura, *Appl. Phys. Lett.* **1999**, *75*, 1473.
- [7] Y. B. Nian, J. Strozier, N. J. Wu, X. Chen, A. Ignatiev, *Phys. Rev. Lett.* **2007**, *98*, 146403/1.
- [8] M. Quintero, P. Levy, A. G. Leyva, M. J. Rozenberg, *Phys. Rev. Lett.* **2007**, *98*, 116601/1.
- [9] A. Sawa, T. Fujii, M. Kawasaki, Y. Tokura, *Appl. Phys. Lett.* **2004**, *85*, 4073.
- [10] S. Dirkmann, M. Hansen, M. Ziegler, H. Kohlstedt, T. Mussenbrock, *Sci. Rep.* **2016**, *6*, 1.
- [11] M. Hansen, M. Ziegler, L. Kolberg, R. Soni, S. Dirkmann, T. Mussenbrock, H. Kohlstedt, *Sci. Rep.* **2015**, *5*, 13753.
- [12] D. S. Jeong, R. Thomas, R. S. Katiyar, J. F. Scott, H. Kohlstedt, A. Petraru, C. S. Hwang, *Rep. Prog. Phys.* **2012**, *75*, 76502/1.
- [13] H. Sim, H. Choi, D. Lee, M. Chang, D. Choi, Y. Son, E. Lee, W. Kim, Y. Park, I. Yoo, H. Hwang, *IEEE Int. Electron Devices Meet., Tech. Dig.* **2005**, 777.
- [14] M. Hasan, R. Dong, H. J. Choe, D. S. Lee, D. J. Seong, M. B. Pyun, H. Hwang, *Appl. Phys. Lett.* **2008**, *92*, 202102.
- [15] A. Baikov, Y. Q. Wang, B. Shen, B. Lorenz, S. Tsui, Y. Y. Sun, Y. Y. Xue, C. W. Chu, *Appl. Phys. Lett.* **2003**, *83*, 957.
- [16] B. Govoreanu, D. Crotti, S. Subhechha, L. Zhang, Y. Y. Chen, S. Clima, V. Paraschiv, H. Hody, C. Adelman, M. Popovici, O. Richard, M. Jurczak, *IEEE Symp. VLSI Technol.* **2015**, T132.
- [17] B. Govoreanu, A. Redolfi, L. Zhang, C. Adelman, M. Popovici, S. Clima, H. Hody, V. Paraschiv, I. P. Radu, A. Franquet, J.-C. Liu, J. Swerts, O. Richard, H. Bender, L. Altissime, M. Jurczak, *IEEE Int. Electron Devices Meet.* **2013**, *13*, 256.
- [18] X. Chen, N. J. Wu, J. Strozier, A. Ignatiev, *Appl. Phys. Lett.* **2005**, *87*, 233506.
- [19] D. J. Seong, M. Jo, D. Lee, H. Hwang, *Electrochem. Solid-State Lett.* **2007**, *10*, H168.
- [20] S. H. Jeon, B. H. Park, J. Lee, B. Lee, S. Han, *Appl. Phys. Lett.* **2006**, *89*, 42904.
- [21] A. Ignatiev, N. J. Wu, X. Chen, Y. B. Nian, C. Papagianni, S. Q. Liu, J. Strozier, *Phase Transitions* **2008**, *81*, 791.
- [22] S. Asanuma, H. Akoh, H. Yamada, A. Sawa, *Phys. Rev. B* **2009**, *80*, 235113/1.
- [23] R. Muenstermann, T. Menke, R. Dittmann, R. Waser, *Adv. Mater.* **2010**, *22*, 4819.
- [24] T. Fujii, M. Kawasaki, A. Sawa, H. Akoh, Y. Kawazoe, Y. Tokura, *Appl. Phys. Lett.* **2005**, *86*, 12107.
- [25] R. Fors, S. I. Khartsev, A. M. Grishin, *Phys. Rev. B* **2005**, *71*, 45305.
- [26] M. J. Rozenberg, I. H. Inoue, M. J. Sanchez, *Phys. Rev. Lett.* **2004**, *92*, 178302/1.
- [27] T. Oka, N. Nagaosa, *Phys. Rev. Lett.* **2005**, *95*, 266403/1.
- [28] K. H. Xue, C. A. P. de Araujo, J. Celinska, C. McWilliams, *J. Appl. Phys.* **2011**, *109*, 91602/1.
- [29] H. S. Lee, S. G. Choi, H. H. Park, M. J. Rozenberg, *Sci. Rep.* **2013**, *3*, 1704/1.
- [30] A. Sawa, *Mater. Today* **2008**, *11*, 28.
- [31] B. Iffland, P. Peretzki, B. Kressdorf, P. Saring, A. Kelling, M. Seibt, C. Jooss, *Beilstein J. Nanotechnol.* **2015**, *6*, 1467.
- [32] K. Shono, H. Kawano, T. Yokota, M. Gomi, *Appl. Phys. Express* **2008**, *1*, 55002/1.
- [33] H. Kawano, K. Shono, T. Yokota, M. Gomi, *Appl. Phys. Express* **2008**, *1*, 101901/1.



- [34] F. Borgatti, C. Park, A. Herpers, F. Offi, R. Egoavil, Y. Yamashita, A. Yang, M. Kobata, K. Kobayashi, J. Verbeeck, G. Panaccione, R. Dittmann, *Nanoscale* **2013**, *5*, 3954.
- [35] A. Herpers, C. Lenser, C. Park, F. Offi, F. Borgatti, G. Panaccione, S. Menzel, R. Waser, R. Dittmann, *Adv. Mater.* **2014**, *26*, 2730.
- [36] R. Meyer, L. Schloss, D. Brewer, R. Lambertson, W. Kinney, J. Sanchez, D. Rinerson, in *Proc. Non-Volatile Memory Technology Symp.* **2008**, p. 54.
- [37] C. J. Chevallier, C. H. Siau, S. F. Lim, S. R. Namala, M. Matsuoka, B. L. Bateman, D. Rinerson, in *Technical Digest ISSCC* **2010**, p. 260.
- [38] K. Gundlach, H. Konishi, *Appl. Phys. Lett.* **1985**, *46*, 441.
- [39] H. Kohlstedt, K. Gundlach, S. Kuriki, *J. Appl. Phys.* **1993**, *73*, 2564.
- [40] M. Sowinska, T. Bertaud, D. Walczyk, S. Thiess, P. Calka, L. Alff, C. Walczyk, T. Schroeder, *J. Appl. Phys.* **2014**, *115*, 204509.
- [41] L. A. Walsh, G. Hughes, P. K. Hurley, J. Lin, J. C. Woicik, *Appl. Phys. Lett.* **2012**, *101*, 241602/1.
- [42] M. Sacchi, F. Offi, P. Torelli, A. Fondacaro, C. Spezzani, M. Cautero, G. Cautero, S. Huotari, M. Grioni, R. Delaunay, M. Fabrizioli, G. Vanko, G. Monaco, G. Paolicelli, G. Stefani, G. Panaccione, *Phys. Rev. B* **2005**, *71*, 155117/1.
- [43] E. Slooten, Z. Zhong, H. J. A. Molegraaf, P. D. Eerkes, S. de Jong, F. Masee, E. van Heumen, M. K. Kruize, S. Wenderich, J. E. Kleibeuker, M. Gorgoi, H. Hilgenkamp, A. Brinkman, M. Huijben, G. Rijnders, D. H. A. Blank, G. Koster, P. J. Kelly, M. S. Golden, *Phys. Rev. B* **2013**, *87*, 85128/1.
- [44] F. Borgatti, I. Bergenti, F. Bona, V. Dedi, A. Fondacaro, S. Huotari, G. Monaco, D. A. MacLaren, J. N. Chapman, G. Panaccione, *Appl. Phys. Lett.* **2010**, *96*, 43306/1.
- [45] T. Bertaud, M. Sowinska, D. Walczyk, C. Walczyk, S. Kubotsch, C. Wenger, T. Schroeder, *E-MRS 2012 Spring Meeting, Symposium M: More Than Moore: Novel Materials Approaches For Functionalized Silicon Based Microelectronics* **2012**, *41*, 12018/1.
- [46] E. Kroeger, A. Petraru, A. Quer, R. Soni, M. Kallaene, N. A. Pertsev, H. Kohlstedt, K. Rossnagel, *Phys. Rev. B* **2016**, *93*, 235415/1.
- [47] T. Watanabe, K. Tada, S. Yasuno, H. Oji, N. Yoshimoto, I. Hirotsawa, *Jpn. J. Appl. Phys.* **2016**, *55*, 3DD12/1.
- [48] S. Park, H. Kim, M. Choo, J. Noh, A. Sheri, S. Jung, K. Seo, J. Park, S. Kim, W. Lee, J. Shin, D. Lee, G. Choi, J. Woo, E. Cha, J. Jang, C. Park, M. Jeon, B. Lee, B. H. Lee, H. Hwang, *IEEE Int. Electron Devices Meet.* **2012**, 232.
- [49] L. Marot, D. Mathys, G. De Temmerman, P. Oelhafen, *Surf. Sci.* **2008**, *602*, 3375.
- [50] M. Pomfret, C. Stoltz, B. Varughese, R. Walker, *Anal. Chem.* **2005**, *77*, 1791.
- [51] A. F. Santander-Syro, O. Copie, T. Kondo, F. Fortuna, S. Pailhes, R. Weht, X. G. Qiu, F. Bertran, A. Nicolaou, A. Taleb-Ibrahimi, P. Le Fevre, G. Herranz, M. Bibes, N. Reyren, Y. Apertet, P. Lecoeur, A. Barthelemy, M. J. Rozenberg, *Nature* **2011**, *469*, 189.
- [52] L. Dudy, M. Sing, P. Scheiderer, J. D. Denlinger, P. Schuetz, J. Gabel, M. Buchwald, C. Schlueter, T. Lee, R. Claessen, *Adv. Mater.* **2016**, *28*, 7443.
- [53] M. Truccato, A. Agostino, E. Borfecchia, L. Mino, E. Cara, A. Pagliero, N. Adhlakha, L. Pascale, L. Operti, E. Enrico, N. De Leo, M. Fretto, G. Martinez-Criado, C. Lamberti, *Nano Lett.* **2016**, *16*, 1669.
- [54] N. Fairley, A. Carrick, *The Casa Cookbook: Recipes for XPS Data Processing, Pt. 1, Vol. 1*, Acolyte Science, Cheshire, UK **2005**.
- [55] L. Garvie, A. Craven, *Phys. Chem. Miner.* **1994**, *21*, 191.
- [56] J. Richter, A. Braun, A. S. Harvey, P. Holtappels, T. Graule, L. Gauckler, *Physica B* **2008**, *403*, 87.
- [57] J. Herrero-Martin, J. L. Garcia-Munoz, S. Valencia, C. Frontera, J. Blasco, A. J. Baron-Gonzalez, G. Subias, R. Abrudan, F. Radu, E. Dudzik, R. Feyerherm, *Phys. Rev. B* **2011**, *84*, 115131/1.
- [58] Z. Hu, G. Kaindl, H. Ogasawara, A. Kotani, I. Felner, *Chem. Phys. Lett.* **2000**, *325*, 241.
- [59] J. Luis Garcia-Munoz, C. Frontera, A. J. Baron-Gonzalez, S. Valencia, J. Blasco, R. Feyerherm, E. Dudzik, R. Abrudan, F. Radu, *Phys. Rev. B* **2011**, *84*, 45104/1.
- [60] D. McComb, *Phys. Rev. B* **1996**, *54*, 7094.
- [61] S. Ostanin, A. Craven, D. McComb, D. Vlachos, A. Alavi, M. Finnis, A. Paxton, *Phys. Rev. B* **2000**, *62*, 14728.
- [62] S. Ostanin, A. J. Craven, D. W. McComb, D. Vlachos, A. Alavi, A. T. Paxton, M. W. Finnis, *Phys. Rev. B* **2002**, *65*, 224109.
- [63] S. Fabris, A. Paxton, M. Finnis, *Acta Mater.* **2002**, *50*, 5171.
- [64] R. French, S. Glass, F. Ohuchi, Y. Xu, W. Ching, *Phys. Rev. B* **1994**, *49*, 5133.
- [65] S. Kobayashi, A. Yamasaki, T. Fujiwara, *Jpn. J. Appl. Phys., Part 1* **2003**, *42*, 6946.
- [66] Y. Chen, N. Pryds, J. E. Kleibeuker, G. Koster, J. Sun, E. Stamate, B. Shen, G. Rijnders, S. Linderoth, *Nano Lett.* **2011**, *11*, 3774.
- [67] S. Schramm, J. Hoffmann, C. Jooss, *J. Phys.: Condens. Matter* **2008**, *20*, 395231.
- [68] J. G. Simmons, *J. Appl. Phys.* **1963**, *34*, 2581.
- [69] C. Lenser, A. Koehl, I. Slipukhina, H. Du, M. Patt, V. Feyer, C. M. Schneider, M. Lezaic, R. Waser, R. Dittmann, *Adv. Funct. Mater.* **2015**, *25*, 6360.
- [70] A. Jablonski, C. J. Powell, *J. Electron Spectrosc. Relat. Phenom.* **1999**, *100*, 137.
- [71] J. Scott, P. J. Thomas, M. MacKenzie, S. McFadzean, J. Wilbrink, A. J. Craven, W. A. P. Nicholson, *Ultramicroscopy* **2008**, *108*, 1586.
- [72] J. Hunt, D. Williams, *Ultramicroscopy* **1991**, *38*, 47.